

Viewpoint article

Thermo-mechanical behavior of organic-inorganic halide perovskites for solar cells



Cristina Ramirez, Srinivas K. Yadavalli, Hector F. Garces, Yuanyuan Zhou, Nitin P. Padture *

School of Engineering, Brown University, Providence, RI 02912, USA

ARTICLE INFO

Article history:

Received 24 December 2017

Accepted 16 February 2018

Available online 20 March 2018

Keywords:

Perovskites

Solar cells

Mechanical properties

Residual stress

Residual strain

ABSTRACT

Organic-inorganic halide perovskites (OIHPs) are a remarkable family of hybrid materials at the heart of the emerging thin-film perovskite solar cells (PSCs) technology and other applications. In this Viewpoint article, in addition to some original experimental results, thermo-mechanical analyses of residual macro- and micro-stresses in OIHP thin films are presented in the context of fracture of both the OIHP layer itself and its interface with the substrate. The implications of mechanical behavior of OIHPs and interfaces on the reliability of PSCs, as well as opportunities for future research directions in this general area, are highlighted.

© 2018 Acta Materialia Inc. Published by Elsevier Ltd. All rights reserved.

Organic-inorganic halide perovskites (OIHPs) are a fascinating family of hybrid materials that defy classical classification (metals, ceramics, polymers) and fall into the hitherto uncharted territory between conventional 'soft' and 'hard' materials [1]. In the general OIHP formula ABX_3 , typically A is an organic cation, methylammonium (CH_3NH_3^+ or MA^+) or formamidinium ($\text{HC}(\text{NH}_2)_2^+$ or FA^+); B is Pb^{2+} , or Sn^{2+} ; and X is Cl^- , Br^- , or I^- (Fig. 1A), and their alloy combinations [2,3]. Although OIHPs were discovered in 1978, and their structural understanding, solution-processing, and properties were further developed in the 1990s [2], they did not find widespread interest until the first reported use of OIHP in thin-film solar cells in 2009 [4]. Since then, enormous amount of research has been devoted to OIHPs and perovskite solar cells (PSCs) worldwide [5–10], and now the record efficiency of laboratory-scale PSC stands at 22.7% [11], rivalling that of commercial Si-based solar cells. The promise of low-cost solution-processed, high-efficiency PSCs, and its potential impact on the global renewable energy landscape, is driving this effort worldwide. Furthermore, it is being discovered that OIHPs possess unique and unprecedented (opto)electronic properties, making them useful in other potential applications [12], such as light-emitting diodes [13], lasers [14], and detectors (photon [15], X-ray [16], nuclear-radiation [17], gas [18]).

The crystal structure of OIHPs (Fig. 1A) is based on inorganic framework resulting from the strong B-X ionic/covalent interactions, whereas the A-X bonding is relatively weak. This inorganic-based framework of the OIHP structure is responsible for OIHPs having microstructures (Fig. 1B) typical of 'hard' materials [1,19]. Fig. 1C is a transmission electron microscope (TEM) image showing MAPbI_3 grains and grain boundaries, and

also a proliferation of defects within the grains [20]. The latter is due to the intrinsic low formation-energy of the defects in OIHPs [20]. These defects, as well as the ultrafast organic-cation rotation dynamics and ion mobility, are responsible for the 'soft' nature of OIHPs [21]. While their 'soft' nature allows them to access the vast, rich field of organic/inorganic chemistry [12,21], the similarity of their microstructures to 'hard' materials provides rich opportunities to discover new materials science of OIHPs [1].

While new OIHP materials, synthesis/processing, and PSC architectures continue to be popular research topics, the research focus has been shifting towards topics such as large-area PSCs, scalable manufacturing, stability, durability, and reliability, which is essential if PSCs are to be deployed commercially in the future [10]. Since PSCs are made of multiple functional layers of a diverse set of materials with vastly different thermal and mechanical properties, PSCs reliability will depend on the thermo-mechanical behavior of the multilayer stacks that are expected to cycle through thermal excursions during manufacturing and service. Also, PSCs will be subjected to externally applied stresses. While interfacial adhesive fracture is an important issue in multilayer PSCs, it has been shown that the brittle OIHP layer itself is quite often the 'weakest link' where cohesive fracture occurs [22,23]. Despite the rising importance of fracture of OIHPs, as it may ultimately control the reliability of PSCs (Fig. 2) [23], research in this area has been extremely scant [22–24].

Mechanical and Thermal Properties of MAPbI_3 OIHP

The mechanical properties (elastic modulus (E) and hardness (H)) and the linear coefficients of thermal expansion (CTEs (α)) of MAPbI_3 , the most widely studied OIHP, have been reported, and are summarized in Tables 1 and 2, respectively. Within these limited experimental data

* Corresponding author.

E-mail address: nitin_padture@brown.edu (N.P. Padture).

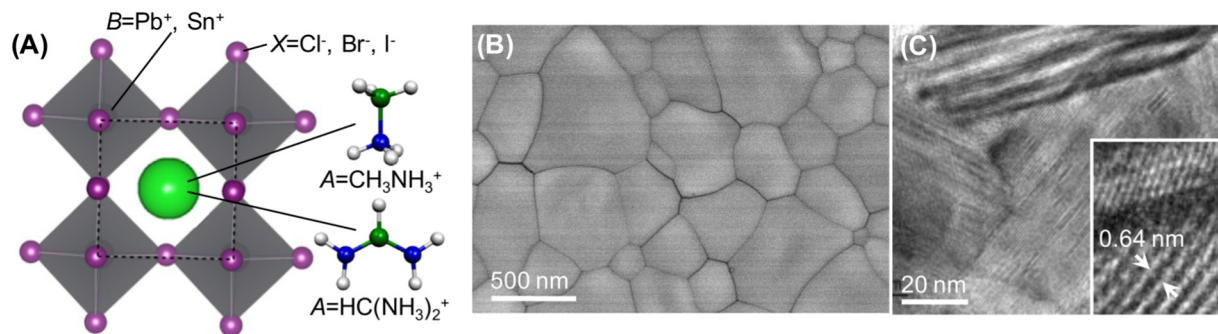


Fig. 1. (A) Schematic illustration of OIHP crystal structure. MAPbI₃ thin film microstructure: (B) SEM image [19] and (C) TEM image showing grain boundaries and defective grains (inset: high-resolution TEM image) [20]. (Adapted with permission from RSC.)

there appears to be some variation. With regards to E and H properties, all the studies on MAPbI₃ are based on the indentation technique [23,25–29], which is highly sensitive to the surface conditions. Also, the E and H measurements depend on the indentation dwell time as MAPbI₃ creeps significantly at room temperature at dwell times as short as 20 s [28]. In the case of CTEs, the origin of the variation could be due to the nature of the samples studied: single-crystals [30], films [31], and powders [32,33]. Nevertheless, the measured CTEs of MAPbI₃ are significantly higher than that of soda-lime silicate glass ($\alpha_{\text{Glass}} \sim 10 \times 10^{-6} \text{ }^{\circ}\text{C}^{-1}$) [34], which is commonly used as the substrate material in PSCs.

Here we have measured E and H values of a carefully prepared MAPbI₃ single-crystal (100 face) using the nanoindentation technique, and they are reported in Table 1 (see Supplementary Information (SI) for experimental details). A Berkovich diamond indenter was used, and the dwell time at peak load was limited to 0.5 s in order to preclude any creep effects [28]. An average E value of 17.8 GPa is obtained using the Oliver and Pharr analysis [35], which is on the high side compared to that reported in the literature (Table 1). At 20-s dwell time, the average E value drops to 12.7 GPa, which is in the ballpark of what others have reported (Table 1). Similarly, the average H values are 0.58 GPa and 0.48 GPa at 0.5 s and 20 s dwell time, respectively. While most papers do not report indentation dwell time, from the reported load-displacement curves it appears that most studies use dwell times approaching

20 s or longer. Our results clearly show that room-temperature indentation creep is important, and, thus, it is recommended that very short dwell time (0.5 s) be used in future indentation experiments to preclude any creep effects that can result in the erroneous underestimation of E and H .

The cohesive fracture energy (Γ_0) of polycrystalline MAPbI₃ thin films has been reported to be in the range 0.24–1.48 J·m⁻² (Table 3), as measured using the double-cantilever-beam delamination test [22,23]. Using E of 17.8 GPa, this translates to a toughness (K_{IC}) range of 0.06–0.16 MPa·m^{0.5}, where $K_{\text{IC}} = (\Gamma_0 E)^{0.5}$ [36]. While these values are comparable to single-crystal NaCl salt (0.15–0.26 MPa·m^{0.5} [22]), they are quite low compared to other brittle inorganic materials used in solar cells such as silicon and glass ($K_{\text{IC}} \sim 0.7 \text{ MPa} \cdot \text{m}^{0.5}$) [36]. In this context, we have used nanoindentation to estimate the K_{IC} values of single-crystal MAPbI₃ OIHP (100 face). A cube-corner diamond indenter is used in order to promote crack formation at a low nanoindentation load (P), and it is aligned to result in cracking along the easy-cleavage plane. The crack size, c , is measured and the K_{IC} is estimated using the following equation: [37]

$$K_{\text{IC}} = \alpha \left(\frac{E}{H} \right)^{0.5} \frac{P}{c^{1.5}}, \quad (1)$$

where the constant α is given by $\{(0.0352 / (1 - \nu)) \times (\cot \Psi)^{0.67}\}$. The included angle Ψ for cube-corner indenter is 35.3°, which is much sharper than that for the Berkovich indenter ($\Psi = 65.3^\circ$), and ν is the Poisson's ratio ($= 0.33$) [25]. Using $E/H = 30.7$ (Table 1), the average K_{IC} is estimated at 0.22 MPa·m^{0.5}. Note that a longer dwell time (20 s) results in an erroneous underestimation of the K_{IC} (Table 3). Recently, Rolston et al. [23] have reported a K_{IC} of 0.15 MPa·m^{0.5} for single-crystal MAPbI₃ OIHP using the Vicker's indentation method (10 s dwell time) [36].

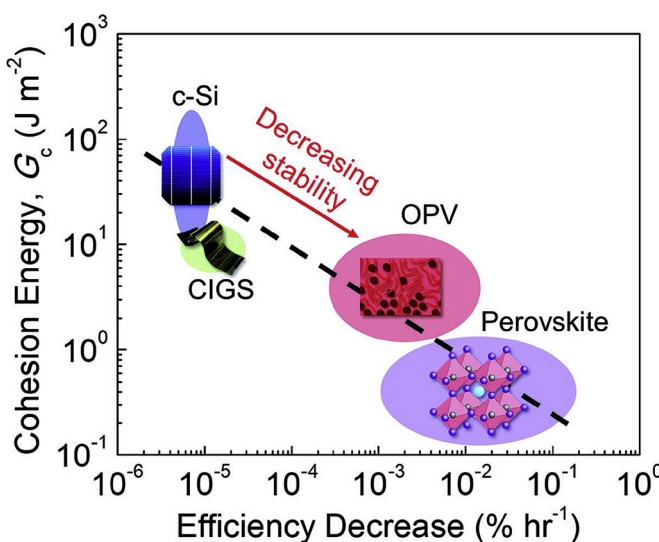


Fig. 2. The measured cohesion, G_c (same as Γ_0), and degradation rate as a function of solar cell active material, showing a correlation between mechanical integrity and long-term reliability [23]. (Adapted with permission from VCH-Wiley.)

Table 1

Elastic modulus and hardness values of single-crystal MAPbI₃ measured using indentation techniques.

E (GPa)	H (GPa)	E/H	Remarks	Ref.
14.3	0.57	25.1	100 face	[25]
14.0	0.55	25.5	112 face	
10.4	0.42	24.8	100 face	[26]
10.7	0.46	23.3	112 face	
20.0	1.0	20.0	–	[27]
10.8	0.55	19.6	100 face	[28]
–	0.47	–	–	[29]
–	–	100 ^a	–	[23]
17.8 ^b	0.58 ^b	30.7 ^b	100 face	This study
12.7 ^c	0.48 ^c	26.5 ^c	100 face	This study

^a Knoop indentation.

^b Dwell time 0.5 s.

^c Dwell time 20 s.

Table 2Linear CTE values of MAPbI_3 and temperature ranges.

Cubic ($^{\circ}\text{C}^{-1}$)	Tetragonal ($^{\circ}\text{C}^{-1}$)	Pseudocubic ($^{\circ}\text{C}^{-1}$)	Remarks	Ref.
$\alpha_a = 42.4 \times 10^{-6}$ (T: 57 to 87 °C)	–	$\alpha_{\text{AVE}} = 44.5 \times 10^{-6}$ ^a (T: –103 to 56 °C)	Single-crystal; CTE extracted	[30]
$\alpha_a = 47.7 \times 10^{-6}$ (T: 54 to 98 °C)	$\alpha_{a,b} = 132 \times 10^{-6}$ $\alpha_c = -106 \times 10^{-6}$ (T: 35 to 51 °C)	$\alpha_{\text{AVE}} = 52.3 \times 10^{-6}$ ^a (T: 35 to 53 °C)	Drop-cast film; CTE reported	[31]
$\alpha_a = 35.1 \times 10^{-6}$ (T: 51 to 77 °C)	–	$\alpha_{\text{AVE}} = 42.4 \times 10^{-6}$ ^b (T: –113 to 52 °C)	Powder; CTE reported	[32,33]

^a Based on volume CTE ($\alpha_{\text{AVE}} = \alpha_{\text{VOL}}/3$).^b Based on tetragonal CTEs ($\alpha_{\text{AVE}} = (2\alpha_a + \alpha_c)/3$).

Now we are placed to perform analyses of residual macro- and micro-stresses in planar OIHP thin films. Considering the paucity of thermal and mechanical properties data for other OIHPs, these analyses are limited to MAPbI_3 thin films as a case study. The upper-bound CTE values from Table 2 are used to calculate the maximum possible residual stresses as the worst-case scenario.

Macroscopic Residual Stresses

Most solution-processed MAPbI_3 thin films are typically crystallized at an elevated temperature (T) of 100–150 °C, and are generally deposited on thick glass substrates having a thin coating of a transparent conduction oxide, typically fluorinated tin oxide (FTO) or indium tin oxide (ITO). Thus, during cooling, the polycrystalline MAPbI_3 thin film is in a state of equi-biaxial in-plane residual tensile stress due to the CTE mismatch with the substrate (assuming perfect film/substrate bonding), which is described as macro-stress (σ_{Macro} ; Fig. 3). Since the thin-film contraction is not constrained by the substrate in the vertical direction, the out-of-plane strain is only due to the Poisson's effect ($\nu = 0.33$), which is a third of the in-plane strain and of the opposite sign. Thus, the out-of-plane residual stress is expected to be zero. Also, the glass substrate is massive (millimeters) compared to the MAPbI_3 thin film (~500 nm) and the FTO/ITO coating (~1 μm), and, therefore, the residual stress generated in the glass substrate is negligible. (Note that this may not be the case in thin, low-E flexible polymer substrates, such as polyethylene terephthalate or PET.) Using 150 °C as the upper bound temperature, and 55 °C as the cubic-to-tetragonal transformation temperature [38,39], the maximum residual σ_{Macro} in a cubic polycrystalline MAPbI_3 thin film on glass substrate at 55 °C ($\Delta T = 150–55 = 95$ °C) is calculated using the following: [40]

$$\sigma_{\text{Macro}} = E\Delta\alpha\Delta T, \quad (2)$$

where $\Delta\alpha = (\alpha_a - \alpha_{\text{Glass}})(47.7 \times 10^{-6} - 10 \times 10^{-6}) = 37.7 \times 10^{-6} ^{\circ}\text{C}^{-1}$. The cubic MAPbI_3 CTE values from Table 2 are used here, but E value corresponding to tetragonal MAPbI_3 (100) we measured ($E = 17.8$ GPa) is used, because E for cubic MAPbI_3 is unknown but it is unlikely to be very different from that of tetragonal MAPbI_3 . During further cooling of the tetragonal MAPbI_3 thin films from 55 °C to room temperature (25 °C;

$\Delta T = 55–25 = 30$ °C), additional σ_{Macro} is generated. Assuming that no significant volume change occurs during the cubic-to-tetragonal transformation at 55 °C [31], and that the polycrystalline MAPbI_3 thin film has randomly-oriented grains, we use $\Delta\alpha = (\alpha_{\text{Ave}} - \alpha_{\text{Glass}}) = (52.3 \times 10^{-6} - 10 \times 10^{-6}) = 42.3 \times 10^{-6} ^{\circ}\text{C}^{-1}$ in Eq. (2) to calculate that additional σ_{Macro} . Thus, the total σ_{Macro} in a typical non-textured polycrystalline MAPbI_3 thin film on a glass substrate at room temperature (cooled from 150 °C) is 86 MPa, corresponding to a maximum biaxial tensile residual strain of 0.49% in the film. If the thin film is cooled down further to –40 °C, the lowest solar-panels test temperature, the total tensile residual σ_{Macro} at –40 °C is 135 MPa. These results are plotted in Fig. 4A as a function of temperature.

The σ_{Macro} in films can induce spontaneous fracture without the application of external stress if a sufficiently large incipient crack exists in the thin film. The critical radius of a half-penny surface crack, c_* , (Fig. 3A) can be calculated using: [36]

$$c_* = \pi \left(\frac{K_{\text{IC}}}{2\sigma_{\text{Macro}}} \right)^2. \quad (3)$$

Using the intrinsic toughness of MAPbI_3 , $K_{\text{IC}} = 0.22 \text{ MPa} \cdot \text{m}^{0.5}$, and the maximum biaxial tensile residual $\sigma_{\text{Macro}} = 135$ MPa (at –40 °C), the calculated c_* value is 2.1 μm. Since typical MAPbI_3 thin films in PSCs are ~500 nm thick, it is impossible to have an incipient crack deeper than the film thickness. However, using the lower bound $K_{\text{IC}} = 0.06 \text{ MPa} \cdot \text{m}^{0.5}$ [22] as the worst-case scenario, the calculated c_* is 154 nm; it is possible to have such incipient flaws in a 500-nm thin film. The c_* values corresponding to the maximum possible σ_{Macro} as a function of temperature are plotted in Fig. 4B. The fact that the c_* -T curve fall below the dashed line (500 nm) only for the worst-case scenario in terms of upper bound σ_{Macro} and lower bound K_{IC} indicates that CTE-mismatch-induced spontaneous cracking (i.e. without the application of external stress) in well-made MAPbI_3 OIHP thin films may not be a big concern. However, if incipient cracks do propagate

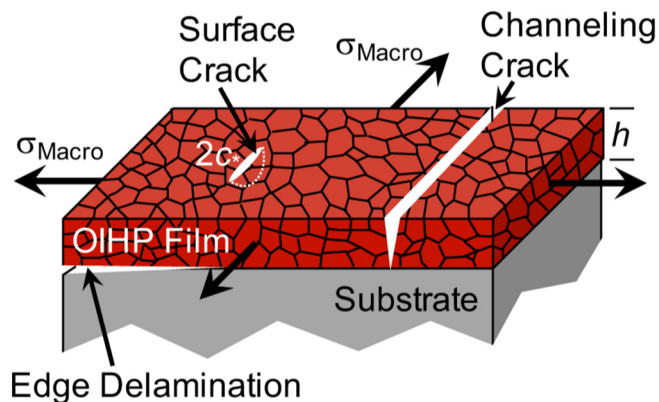


Fig. 3. Schematic illustration of polycrystalline (non-textured) OIHP thin film under equi-biaxial tensile residual macro-stress (σ_{Macro}), with 'half-penny' critical surface crack (diameter $2c_*$), channeling crack ($c = h$), and edge delamination.

Table 3Fracture energy and toughness of MAPbI_3 thin films and single-crystals.

Γ_0 ($\text{J} \cdot \text{m}^{-2}$)	K_{IC} ($\text{MPa} \cdot \text{m}^{0.5}$)	Remarks	Ref.
0.24	0.06 ^a	Capping-layer on mesoscopic film	[22]
1.48	0.16 ^a	Planar film	[22]
0.83	0.12 ^a	Slot-die-coated film	[23]
1.26 ^a	0.15	Single-crystal Vicker's indentation	[23]
2.72 ^{a,b}	0.22 ^b	Single-crystal (100 face) cube-corner nanoindentation	This study
1.82 ^{a,c}	0.18 ^c		This study

^a Calculated using $E = 17.8$ GPa.^b Dwell time 0.5 s.^c Dwell time 20 s.

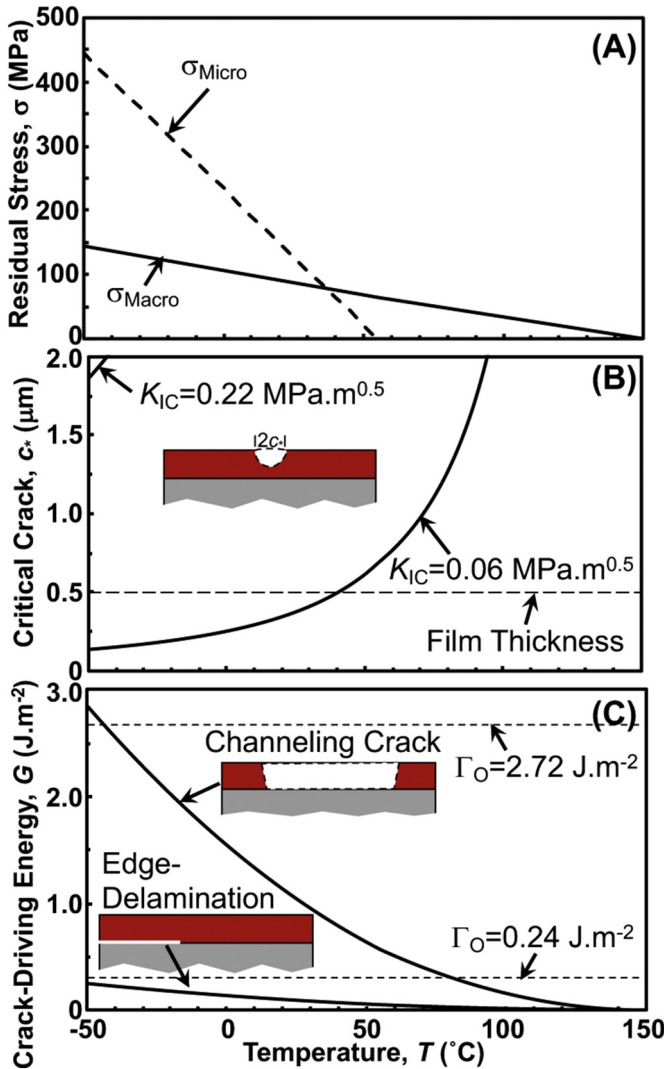


Fig. 4. (A) Calculated maximum possible tensile residual σ_{Macro} and σ_{Micro} in a non-textured polycrystalline MAPbI₃ thin film as a function of temperature of the film cooled from 150 °C. (B) Calculated ‘half-penny’ critical surface crack radii (c_*) in the above film corresponding to σ_{Macro} from (A) using upper and lower bound K_{IC} values. Dashed horizontal line indicates film thickness of ~500 nm, c_* above which have no physical meaning. (C) Calculated crack-driving energy, G , for channeling crack and edge delamination using σ_{Macro} from (A). Dashed lines in (C) indicate upper and lower bounds Γ_{O} values.

through-thickness of the film, they will be arrested at the interface because the substrate is significantly tougher. However, they can channel across the film (Fig. 3), the condition for which is given by: [41]

$$G = \frac{c_e^2 \pi h \sigma_{\text{Macro}}^2}{E} \geq \Gamma_{\text{O}}, \quad (4)$$

where G crack-driving energy (strain energy release rate) and c_e is a constant ($=1.258$). Assuming a film thickness $h = 500$ nm and using σ_{Macro} from Fig. 4A, G as a function of temperature is plotted in Fig. 4C. Since Eq. (5) is satisfied even for upper bound Γ_{O} at low temperatures, through-thickness cracks of radius $c = h$ (propagated from c_* or pre-existing in the film) are likely to channel along the film. Note that due to the equi-biaxial nature of the residual stress, multiple channelling cracks can propagate in different directions creating a ‘mudflat’ cracking pattern. The residual tensile σ_{Macro} can also induce mode-II edge delamination of the MAPbI₃ thin film from the substrate (Fig. 3), condition for which is given by: [41,42]

$$G = \frac{(1-\nu^2) h \sigma_{\text{Macro}}^2}{2E} \geq \Gamma_i, \quad (5)$$

where Γ_i is the interfacial adhesive fracture energy. Assuming a film thickness $h = 500$ nm and using σ_{Macro} from Fig. 4A, G as a function of temperature is also plotted in Fig. 4C. Since $\Gamma_i > \Gamma_{\text{O}}$ in most cases, as evinced by the fact that fracture occurs within the MAPbI₃ layer and not at the interface [22,23], and G is below the lower bound Γ_{O} , interfacial adhesive fracture is unlikely to occur due to σ_{Macro} in well-adhered MAPbI₃ thin films.

Note that the 150 °C film-formation temperature used in these calculations is on the high side, and some mechanical attachment between the crystallizing film and the substrate may occur at lower temperatures during deposition. Thus, the maximum σ_{Macro} calculated above are likely to be overestimates. Also note that fully-crystalline MAPbI₃ thin films can be deposited at or near room-temperature using scalable methods such as antisolvent-solvent extraction [43] and gas-induced formation and transformation (GIFT) [21,44], where no further heat-treatment is required. In those cases, σ_{Macro} at room temperature is expected to be zero. For a temperature excursion to -40 °C ($\Delta T = |-40 - 25| = 65$ °C), the residual tensile σ_{Macro} is calculated to be 49 MPa.

The anisotropic CTE of tetragonal MAPbI₃ below 55 °C has implications on the σ_{Macro} residual stresses if the films are textured. It has been observed that some solution-processed MAPbI₃ thin films have a 110 “mosaic” texture [21,44,45], which implies that the c -axis of the tetragonal MAPbI₃ grains is parallel to the film/substrate interface while the a/b axes are not. Using $\Delta\alpha = (\alpha_c - \alpha_{\text{Glass}}) = (-106 \times 10^{-6} - 10 \times 10^{-6}) = -116 \times 10^{-6}$ °C⁻¹, a compressive biaxial residual σ_{Macro} is calculated to be -62 MPa for $\Delta T = 55 - 25 = 30$ °C. Thus, the total σ_{Macro} in a typical 110-textured polycrystalline MAPbI₃ thin film at room temperature (cooled from 150 °C) is 2 MPa, which is negligible. Thus, there is a clear advantage in having 110 ‘mosaic’ texture in polycrystalline MAPbI₃ thin films.

In order to determine the σ_{Macro} experimentally, we fabricated a non-textured MAPbI₃ thin film (~500 nm) on a glass substrate using the ‘solvent engineering’ method (heat-treated at 150 °C) [46]. The equi-biaxial residual tensile stresses in this film were measured at room temperature using the established and reliable X-ray diffraction (XRD) $\sin^2\psi$ method on a high-resolution diffractometer [47]. (See SI for experimental details.) Fig. 5 plots the d_{134} planar spacing as a function of $\sin^2\psi$ for a film in two orthogonal orientations ($\phi = 0^\circ$ and 90°). The residual stress is calculated using the following: [47]

$$\sigma_{\text{Macro}} = \left(\frac{E}{1-\nu} \right)_{<134>} \left(\frac{m}{d_0} \right), \quad (6)$$

where m is the slope of the linear fit to the data in Fig. 5 and d_0 is the stress-free d_{134} spacing, which is estimated using the y -intercept. Since the elastic constants of MAPbI₃ in the $\langle 134 \rangle$ directions are not known, the average values for E (=17.8 GPa) and ν (=0.33) are used, which is a good approximation considering that $\{134\}$ are high-index planes. The bi-axial residual tensile σ_{Macro} are found to be 42 MPa and 35 MPa for $\phi = 0^\circ$ and 90° , respectively, which is quite uniform. These

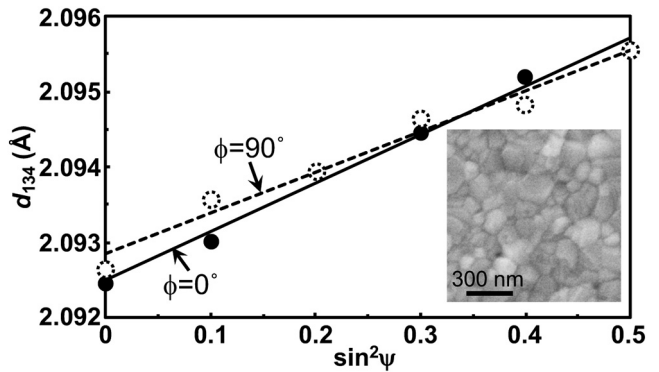


Fig. 5. XRD $\sin^2\psi$ plots (at two orthogonal orientations) for MAPbI₃ thin film heat-treated at 150 °C (inset: film top-surface SEM micrograph).

values are rather small (corresponding to ~0.22% average residual tensile strain) and are less than half of the calculated one, but as discussed earlier, the calculated σ_{Macro} is an overestimation. In this context, recently Zhao et al. [48] have used simple peak shifts in XRD patterns of MAPbI₃ thin films (annealed at 100 °C), compared to powder samples, to estimate a CTE-mismatch strain of 0.47%.

Microscopic Residual Stresses

The anisotropic CTE will also lead to the generation of localized residual micro-stresses, σ_{Micro} , at grain boundaries in polycrystalline tetragonal MAPbI₃ thin films as they are cooled from 55 °C to room temperature and below. This is in addition to the overall σ_{Macro} , which will be superimposed on the local σ_{Micro} . At this juncture, it is instructive to discuss the nature of the cubic-to-tetragonal transformation in MAPbI₃. This phase transformation is displacive (diffusionless), involving cooperative tilting of the PbI₆ octahedra around 001 (one-tilt system, $a^0a^0c^-$ in Glazer notation) with respect to the parent cubic phase (Fig. 6A) [30]. Now consider a polycrystalline MAPbI₃ OIHP thin film in the cubic phase just above 55 °C with randomly-oriented grains (Fig. 6B). The σ_{Micro} is zero at any grain boundary since the CTE (a second rank tensor) of the cubic phase is isotropic (Fig. 6B). Assuming that the entirety of each cubic grain transforms to a corresponding tetragonal grain, the tetragonal unit cell can form with its *c*-axis aligned along any of the three axes of its parent cubic phase. Thus, the tetragonal grain can have six possible crystallographically-equivalent orientations with respect to its parent cubic grain, making it a ferroelastic material by definition [49]. Upon further cooling, although the unit-cell volume-contraction is similar to the cubic unit cell, σ_{Micro} will start to build up at the grain boundaries between adjacent grains due to the CTE anisotropy (Fig. 6B). (Note that in a non-textured polycrystalline material all the individual σ_{Micro} will add up to zero overall [40].) The magnitude of σ_{Micro} at individual grain boundaries will depend on the misorientation between the adjacent grains. The best-case scenario is when the *c*-axes of adjacent grains are aligned, where σ_{Micro} is expected to be zero. The worst-case scenario is when the *c*-axis of a grain is aligned with the *a/b* axis of the neighboring grain (Fig. 5B). In that case, $\Delta\alpha = (\alpha_c - \alpha_{a,b}) = |(-106 \times 10^{-6} - 132 \times 10^{-6})| = 238 \times 10^{-6} \text{ }^\circ\text{C}^{-1}$, and using $\Delta T = (55-25) = 30 \text{ }^\circ\text{C}$, σ_{Micro} at room temperature is calculated to be 127 MPa. In the case of cooling to -40 °C, the σ_{Micro} is calculated to be

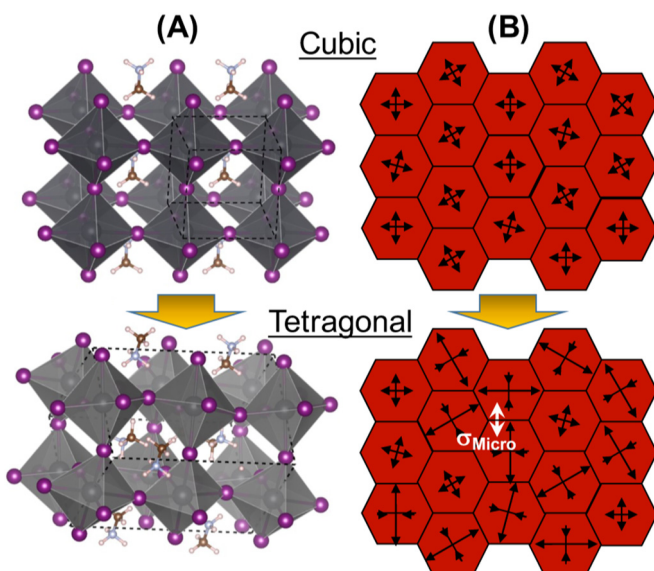


Fig. 6. Schematic illustrations of: (A) the cubic-tetragonal transformation in a perovskite and (B) a polycrystalline (not textured) microstructure showing isotropic CTE in cubic phase (top) and anisotropic CTE in the tetragonal phase (bottom) perovskite. Arrows in (B) not to scale.

403 MPa, which is significant. The σ_{Micro} will superimpose on σ_{Macro} (Fig. 4A), but σ_{Micro} alone can induce grain-boundary microcracks in the film, where critical grain-boundary flaws will propagate, however, they will arrest as they run into compression at neighboring grain-boundaries [40]. However, although a large maximum σ_{Micro} is calculated in non-textured MAPbI₃ thin films above, it is unlikely to be sustained. This is because σ_{Micro} can force the formation of the different orientational variants (ferroelastic domains) within individual grains in order to accommodate the CTE-anisotropy-induced residual strain, thereby reducing the maximum σ_{Micro} . Thus, microcracking is also unlikely to be a major issue in MAPbI₃ thin films. (Note that grain-boundary cracks are often seen in SEM images of MAPbI₃ films in the literature (e.g. Fig. 1B), but they are typically induced by the electron-beam during the SEM observation, and, therefore, are an artifact [50].)

The domains formation in the form of intersecting ‘stripes’ is the hallmark of ferroelastic materials [49], and unsurprisingly it has been observed in MAPbI₃ thin films [51–53], and also in single-crystals [53]. While all the ferroelastic domains are crystallographically equivalent and have the same energy, they can be switched by applying mechanical stress, again, a unique property of ferroelastic materials. Since ferroelastic materials exhibit stress-strain hysteresis, there is a minimum required stress to switch the domains – the coercive stress. This raises the intriguing possibility of toughening MAPbI₃ using ferroelastic switching. Reversible ferroelastic toughening has been established in some ceramics [54], with the most prominent example being Y₂O₃-stabilized ZrO₂ used in thermal barrier coatings for jet-engine components [55]. Here, the stress field ahead of the crack tip causes ferroelastic-domain switching, thereby absorbing the applied mechanical energy that would have otherwise gone into crack propagation, *i.e.* toughening. However, if the coercive stress threshold is not reached in the crack-tip stress field, then toughening will not occur. In general, higher intrinsic fracture resistance (Γ_0) results in higher stresses in the crack-tip field, triggering ferroelastic toughening: $\Gamma = \Gamma_0(1 + \Gamma_{FE})$, where Γ is the total steady-state fracture resistance and Γ_{FE} is the contribution from ferroelastic toughening. Unfortunately, the intrinsic Γ_0 of MAPbI₃ is low (~2.7 J·m⁻² (Table 1), compared with ~6 J·m⁻² for YSZ ceramic [36]), and, therefore, it remains to be seen if there is a window of stress states where MAPbI₃ can be ferroelastically toughened. In this context, other toughening approaches are being pursued. For example, infiltrating MAPbI₃-based OIHP into porous oxides/carbon results in an unprecedented Γ_0 in excess of 3 J·m⁻², which is attributed to the composite-like structure that shields the OIHP from the mechanical loads [23]. Of course, as the OIHP layers are toughened, fracture will occur in the next weakest layer or interface [22].

Other Considerations

Similar analyses can be performed on other OIHPs such as α -FAPbI₃ and its alloys. The α -FAPbI₃ phase, which has a more desirable band gap compared to MAPbI₃ for single-junction solar cells, is cubic [56]. Thus, α -FAPbI₃-based thin films will not have residual micro-stresses (σ_{Micro}) and ferroelasticity. The mechanical [57] and CTE [58,59] properties needed for the thermo-mechanical analyses of these materials have become available, and they appear to be quite similar to those of MAPbI₃. Most recently, Γ_0 values for various (MA,FA,Cs)PbI₃ alloy OIHP thin films have been measured, but they appear to be rather low (0.25–0.59 J·m⁻²) [23].

The thermomechanical analyses so far have been linear elastic. OIHPs will deform plastically when the residual shear stress exceeds the yield strength (τ_y), which is estimated at 370 MPa for single-crystal MAPbI₃ [28]. The maximum residual shear stress in a thin film with the maximum estimated biaxial tensile stress of $\sigma_{Macro} = 135 \text{ MPa}$ is $\tau_{Max} = \sigma_{Macro}/2 = 67.5 \text{ MPa}$, which is much smaller than the τ_y . Thus, σ_{Macro} is unlikely to induce plastic deformation of MAPbI₃ thin films.

While the above analyses are performed only for CTE-mismatch/anisotropy-induced residual stresses and spontaneous cracking/delamination, they can be extended to situations where additional applied

stresses (σ_{App}) are superimposed. The σ_{App} on the OIHP thin films and interfaces can result from flexing, peeling, constraint, etc. during manufacturing, device-packaging, handling, and in-service. The σ_{App} may be more severe compared to residual σ_{Macro} and σ_{Micro} , which can cause serious fracture damage and attendant degradation of the devices. For example, most recently it has been shown that the use of a stiff PSCs encapsulation material, which provides added constraint, is more detrimental to the thermal-cycling performance of the PSCs compared to when a more compliant encapsulation material is used [60].

Outlook

In closing, this Viewpoint article has only scratched the surface regarding the thermo-mechanical behavior of OIHP thin films. If past experience in achieving unprecedented reliability in commercial wafer and thin-film multilayer solar cells is any guide, the reliability of the multilayer PSCs will become critically important as they are poised for commercial deployment. This will make further studies of, not only thermo-mechanical behavior of OIHPs themselves, but also the whole PSC multilayer, indispensable. This presents rich opportunities for future experimental and computational research in topics including, but not limited to: (1) mechanical properties (elastic, plastic, fracture, toughening, creep, fatigue) of OIHPs and interfaces; (2) environmental effects on mechanical properties of OIHPs and interfaces; (3) OIHP thermal properties (expansion, conductivity); (4) *in situ* characterization of residual and applied stresses/strains, and deformation/failure; (5) OIHP microstructural effects (grain size, texture, grain-boundary engineering); (6) OIHP composition/phase/structural-dimensionality effects; (7) chemo-mechanical effects (diffusion, degradation, synthesis/processing); (8) photo-mechanical effects; (9) thermo-mechanical behavior of interfaces in multilayers; and (10) overall device reliability.

Acknowledgements

This research is supported by the Office of Naval Research (N00014-17-1-2232) and the National Science Foundation (OIA-1538893). Experimental assistance from Dr. Y. Lu in performing the nanoindentation tests is gratefully acknowledged.

Appendix A. Supplementary information

Supplementary information to this article can be found online at <https://doi.org/10.1016/j.scriptamat.2018.02.022>.

References

- [1] Y. Zhou, O.S. Game, S. Pang, N.P. Padture, *J. Phys. Chem. Lett.* 6 (2015) 4827–4839.
- [2] D.B. Mitzi, in: K.D. Karlin (Ed.), *Progress in Inorganic Chemistry*, John Wiley & Sons, New York, NY, 1999.
- [3] B. Saparov, D.B. Mitzi, *Chem. Rev.* 116 (2016) 4558–4596.
- [4] A. Kojima, T. Teshima, Y. Shirai, T. Miyasaka, *J. Am. Chem. Soc.* 131 (2009) 6050–6051.
- [5] H.-S. Kim, C.-R. Lee, J.-H. Im, K.-B. Lee, T. Moehl, A. Marchioro, S.-J. Moon, R. Humphrey-Baker, J.-H. Yum, J.E. Moser, M. Grätzel, N.-G. Park, *Sci. Rep.* 2 (2012) 591.
- [6] M.M. Lee, J. Teuscher, T. Miyasaka, T.N. Murakami, H.J. Snaith, *Science* 338 (2012) 643–647.
- [7] M. Liu, M.B. Johnston, H.J. Snaith, *Nature* 501 (2013) 395–398.
- [8] J.H. Heo, S.H. Im, J.H. Noh, T.N. Mandal, C.-S. Lim, J.A. Chang, Y.H. Lee, H.-J. Kim, A. Sarkar, M.K. Nazeeruddin, M. Grätzel, S.I. Seok, *Nat. Photonics* 7 (2013) 486–491.
- [9] N.-G. Park, M. Grätzel, T. Miyasaka, *Organic-inorganic Halide Perovskite Photovoltaics: From Fundamentals to Device Architectures*, Springer, Zurich, Switzerland, 2016.
- [10] J.-P. Correa-Baena, M. Saliba, T. Buonassisi, M. Grätzel, A. Abate, W. Tress, A. Hagfeldt, *Science* 358 (2017) 739–744.
- [11] NREL, www.nrel.gov/ncpv/images/efficiency_chart.jpg 2017.
- [12] Y. Zhao, K. Zhu, *Chem. Soc. Rev.* 45 (2016) 655689.
- [13] Z.-K. Tan, R.S. Moghaddam, M.L. Lai, P. Docampo, R. Higler, F. Deschler, M. Price, A. Sadhanai, L.M. Pazos, D. Credgington, F. Hanusch, T. Bein, H.J. Snaith, R.H. Friend, *Nat. Nanotechnol.* 9 (2014) 687–692.
- [14] G. Xing, N. Matthews, S.S. Lim, N. Yantara, X. Liu, D. Sabba, M. Grätzel, S. Mhaisalkar, T.C. Sum, *Nat. Mater.* 13 (2014) 476–480.
- [15] L. Dou, Y. Yang, J. You, Z. Hong, W.-H. Chang, G. Li, Y. Yang, *Nat. Commun.* 5 (2014) 5404.
- [16] S. Yakunin, M. Sytnyk, D. Kriegner, S. Shrestha, M. Richter, G.J. Matt, H. Azimi, C. Brabec, J. Stangl, M.V. Kovalenko, W. Heiss, *Nat. Photonics* 9 (2015) 444–449.
- [17] Q. Dong, Y. Fang, Y. Shao, P. Mulligan, J. Qiu, L. Cao, J. Huang, *Science* 347 (2015) 967–970.
- [18] C. Bao, J. Yang, W. Zhu, X. Zhou, H. Gao, F.M. Li, G. Fu, T. Yu, Z. Zou, *Chem. Commun.* 51 (2015) 15426–15429.
- [19] H. Hu, D. Wang, Y. Zhou, J. Zhang, S. Lv, S. Pang, X. Chen, Z. Liu, N.P. Padture, G. Cui, *RSC Adv.* 4 (2014) 28964–28967.
- [20] Y. Zhou, M. Yang, A.L. Vasiliev, H.F. Garces, Y. Zhao, D. Wang, S. Pang, K. Zhu, N.P. Padture, *J. Mater. Chem. A* 3 (2015) 9249–9256.
- [21] Y. Zhou, N.P. Padture, *ACS Energy Lett.* 2 (2017) 2166–2176.
- [22] N. Rolston, B.L. Watson, C.D. Bailie, M.D. McGehee, J.P. Bastos, R. Gehlhaar, J.-E. Kim, D. Vak, A.T. Mallajosyula, G. Gupta, A.D. Mohite, R.H. Dauskardt, *Extreme Mech. Lett.* 9 (2016) 353–358.
- [23] N. Rolston, A.D. Printz, J.M. Tracy, H.C. Weerasringhe, D. Vak, L.J. Haur, A. Priyadarshi, N. Mathews, D.J. Slotcavage, M.D. McGehee, R.E. Kalan, K. Zielinski, R.L. Grimm, H. Tsai, W. Nie, A.D. Mohite, S. Gholipour, M. Saliba, M. Grätzel, R.H. Dauskardt, *Adv. Energy Mater.* (2018) (in press) <https://doi.org/10.1002/aenm.201702116>.
- [24] J.-H. Kim, I. Lee, T.-S. Kim, N. Rolston, B.L. Watson, R.H. Dauskardt, *MRS Bull.* 42 (2017) 115–123.
- [25] Y. Rakita, S.R. Cohen, N.K. Kedem, G. Hodes, D. Cahen, *MRS Commun.* (2015) 1–7.
- [26] S. Sun, Y. Fang, G. Kieslich, T.J. White, A.K. Cheetham, *J. Mater. Chem. A* 3 (2015) 18450–18455.
- [27] M. Spina, A. Karimi, W. Andreoni, C.A. Pignedoli, B. Nafradi, L. Forro, E. Horvath, *Appl. Phys. Lett.* 110 (2017), 121903.
- [28] M.A. Reyes-Martinez, A.L. Abdelhady, M.I. Saidaminov, D.Y. Chung, O.K. Bakr, M.G. Kanatzidis, W.O. Soboyejo, Y.-L. Loo, *Adv. Mater.* 29 (2017), 1606556.
- [29] S. Shreshtha, R. Fischer, G.J. Matt, P. Feldner, T. Michel, A. Osvert, I. Levchuk, B. Merle, S. Golkar, H. Chen, S.F. Tedde, O. Schmidt, R. Hock, M. Ruehrig, M. Goeken, W. Heiss, G. Anton, C.J. Brabec, *Nat. Photonics* 11 (2017) 436–440.
- [30] Y. Kawamura, H. Mashiyama, K. Hasebe, *J. Phys. Soc. Jpn.* 71 (2002) 1694–1697.
- [31] T.J. Jacobsson, L.J. Schwan, M. Ottosson, A. Hagfeldt, T. Edvinsson, *Inorg. Chem.* 54 (2015) 10678–10685.
- [32] P.S. Whitefield, N. Herron, W.E. Guise, K. Page, Y.Q. Cheng, I. Milas, M.K. Crawford, *Sci. Rep.* 6 (2016) 35685.
- [33] P.S. Whitefield, N. Herron, W.E. Guise, K. Page, Y.Q. Cheng, I. Milas, M.K. Crawford, *Sci. Rep.* 7 (2016) 42831.
- [34] N.P. Bansal, R.H. Doremus, *Handbook of Glass Properties*, Academic Press, New York, NY, 1986.
- [35] W.C. Oliver, G.M. Pharr, *J. Mater. Res.* 7 (1992) 1564–1583.
- [36] B.R. Lawn, *Fracture of Brittle Solids*, Second Edition Cambridge University Press, Cambridge, UK., 1993.
- [37] J.-J. Jang, G.M. Pharr, *Acta Mater.* 56 (2008) 4458–4469.
- [38] A. Poglitsch, D. Weber, *J. Chem. Phys.* 87 (1987) 6373–6378.
- [39] C.C. Stoumpos, C.D. Malliakas, M.G. Kanatzidis, *Inorg. Chem.* 52 (2013) 9019–9038.
- [40] D.G. Green, *An Introduction to the Mechanical Properties of Ceramics*, Cambridge University Press, Cambridge, UK, 1998.
- [41] L.B. Freund, S. Suresh, *Thin Film Materials: Stress, Defect Formation and Surface Evolution*, Cambridge University Press, Cambridge, UK, 2003.
- [42] H.H. Yu, M.Y. He, J.W. Hutchinson, *Acta Mater.* 49 (2001) 93–107.
- [43] Y. Zhou, M. Yang, W. Wu, A.L. Vasiliev, K. Zhu, N.P. Padture, *J. Mater. Chem. A* 3 (2015) 8178–8184.
- [44] Z. Zhou, Z. Wang, Y. Zhou, S. Pang, D. Wang, H. Xu, Z. Liu, N.P. Padture, G. Cui, *Angew. Chem. Int. Ed.* 54 (2015) 9705–9709.
- [45] F.Ji, S. Pang, L. Zhang, Y. Zong, G. Cui, N.P. Padture, Y. Zhou, *ACS Energy Lett.* 2 (2017) 2727–2733.
- [46] N.J. Jeon, J.H. Noh, Y.C. Kim, W.S. Yang, S. Ryu, S.I. Seok, *Nat. Mater.* 9 (2014) 897–903.
- [47] B.D. Cullity, *Elements of X-ray Diffraction*, Second Edition Addison-Wesley, Boston, MA, 1978.
- [48] J. Zhao, Y. Deng, H. Wei, X. Zheng, Z. Yu, Y. Shao, J.E. Shield, J. Huang, *Sci. Adv.* 3 (2017) eaao5616.
- [49] M.E. Lines, A.M. Glass, *Principles and Applications of Ferroelectrics and Related Materials*, Clarendon Press, Oxford, UK, 1977.
- [50] M. Yang, Y. Zhou, Y. Zeng, C.-S. Jiang, N.P. Padture, K. Zhu, *Adv. Mater.* 27 (2015) 6363–6370.
- [51] I.A. Hermes, S.A. Bretschneider, V.W. Bergman, L.D.A. Klasen, J. Mars, W. Tremel, F. Laquai, H.-J. Butt, M. Mezger, R. Berger, B.J. Rodriguez, S.A.L. Weber, *J. Phys. Chem. C* 120 (2016) 5724–5731.
- [52] M.U. Rothman, W. Li, Y. Zhu, U. Bach, L. Spiccia, J. Etheridge, Y.-B. Cheng, *Nat. Commun.* 8 (2017) 14547.
- [53] E. Strelcov, Q. Dong, T. Li, J. Chae, Y. Shao, Y. Deng, A. Gruverman, J. Huang, A. Centrone, *Sci. Adv.* 3 (2017), e1602165.
- [54] C. Mercer, J.R. Williams, D.R. Clarke, A.G. Evans, *Proc. Roy. Soc. A* 463 (2007) 1393–1408.
- [55] N.P. Padture, *Nat. Mater.* 15 (2016) 804–809.
- [56] M.T. Weller, O.J. Weber, J.M. Frost, A. Walsh, *J. Phys. Chem. Lett.* 6 (2015) 3209–3212.
- [57] S. Sun, F.H. Isikgor, Z. Deng, F. Wei, G. Kieslich, P.D. Bristowe, J. Ouyang, A.K. Cheetham, *SusChemSus* 10 (2017) 3740–3745.
- [58] D.H. Fabini, C.C. Stoumpos, G. Laurita, A. Klitzoglou, A.G. Kontos, P. Falaras, M.G. Kanatzidis, R. Sheshadri, *Angew. Chem. Int. Ed.* 55 (2016) 15392–15396.
- [59] M.T. Weller, O.J. Weber, P.F. Henry, A.M.D. Pumbo, T.C. Hansen, *Chem. Commun.* 51 (2015) 4180–4183.
- [60] R. Cheacharon, N. Rolston, D. Harwood, K.A. Bush, R.H. Dauskardt, M.D. McGehee, *Energy Environ. Sci.* 11 (2018) 144–150.